NANO · MICRO small
www.small-journal.com

Check for updates

Single Iron Site Nanozyme for Ultrasensitive Glucose Detection

Min Chen, Huang Zhou, Xiaokang Liu, Tongwei Yuan, Wenyu Wang, Chao Zhao, Yafei Zhao, Fangyao Zhou, Xin Wang, Zhenggang Xue, Tao Yao, Can Xiong, and Yuen Wu**

Nanomaterials with enzyme-mimicking characteristics have engaged great awareness in various fields owing to their comparative low cost, high stability, and large-scale preparation. However, the wide application of nanozymes is seriously restricted by the relatively low catalytic activity and poor specificity, primarily because of the inhomogeneous catalytic sites and unclear catalytic mechanisms. Herein, a support-sacrificed strategy is demonstrated to prepare a single iron site nanozyme (Fe SSN) dispersed on the porous N-doped carbon. With well-defined coordination structure and high density of active sites, the Fe SSN performs prominent peroxidase-like activity by efficiently activating H_2O_2 into hydroxyl radical (•OH) species. Furthermore, the Fe SSN is applied in colorimetric detection of glucose through a multienzyme biocatalytic cascade platform. Moreover, a low-cost integrated agarose-based hydrogel colorimetric biosensor is designed and successfully achieves the visualization evaluation and quantitative detection of glucose. This work expands the application of single-site catalysts in the fields of nanozyme-based biosensors and personal biomedical diagnosis.

Nanozymes, a class of biomimetic nanomaterials exhibiting intrinsic enzyme-mimicking characteristics,[1–3] have attracted widespread attentions as potential alternatives to natural enzymes owing to the merits of large-scale preparation, low cost, and high stability under harsh conditions.[4] In recent years, various nanozymes with inherent oxidase,[5] peroxidase,[6] superoxide dismutase,[7] and catalase-like[8] activities have been explored and extensively applied in biosensors,[9] clinical medicine,[10] and environmental treatment.[11] Nevertheless, many reported nanozymes such as metal oxides suffer from lower activity and poorer specificity compared with natural enzymes, due to the inhomogeneous elemental composition and low densities of catalytic activity sites,[12] which seriously hinders the practical application of nanozymes. To address these challenges, size reduction,[13] surface modification,[14] structure alteration,[15] and composition optimization[16] have been proposed to optimize nanozymes, but still far from satisfactory. For example, size reduction of nanoparticles always leads to the increase in surface free energy, resulting in serious aggregation and rapid loss of activity. Surface modification of nanozymes may shield some active sites on the surface, leading to low atomic utilization. Thus, it is highly desired to synthesize a new type of nanozymes with homogeneous atomic composition and high densities of activity sites.

As reported, single-site catalysts (SSCs) can provide more opportunities to bridge the gap between natural enzymes and nanozymes due to the maximum atomic utilization efficiency and the well-defined coordination structure.[17–22] Inspired by this, herein, we propose a new self-supporting atomically dispersed single iron site nanozyme (Fe SSN) with high peroxidase-like performance, prepared by a support-sacrificed strategy (**Figure 1**a). In brief, ferrous acetate ($Fe(OAc)_2$) reacted with 1,10-phenanthroline monohydrate (O-phen) in ethanol to form a $Fe(phen)_x$ complex. Followed by adding magnesium oxide powder (MgO), the as-prepared hybrid sample ($Fe(phen)_x$/MgO) was dried and pyrolyzed at 600 °C in Ar atmosphere to get Fe–N–C/MgO. Finally, MgO support was removed by acid pickling and Fe SSN was obtained. The color evolution during the preparation of Fe SSN can be seen in Figure S1 in the Supporting Information. Fe SSN showed no magnetic property under the external magnet (Figure S1d, Supporting Information). Given that Fe SSN can effectively catalyze colorless 3,3′,5,5′-tetramethylbenzidine (TMB) to blue oxidased TMB (ox-TMB) in the presence of H_2O_2, we successfully achieved highly sensitive and selective determination of glucose through modified

M. Chen, H. Zhou, W. Wang, C. Zhao, Y. Zhao, F. Zhou, Dr. X. Wang, Z. Xue, Dr. C. Xiong, Prof. Y. Wu
Department of Chemistry
Hefei National Laboratory for Physical Sciences at the Microscale
iChEM (Collaborative Innovation Center of Chemistry for Energy Materials)
University of Science and Technology of China
Hefei 230026, China
E-mail: canxiong@ustc.edu.cn; yuenwu@ustc.edu.cn
X. Liu, Prof. T. Yao
National Synchrotron Radiation Laboratory
University of Science and Technology of China
Hefei 230026, China
T. Yuan
Research School of Chemistry
Australian National University
Canberra, ACT 2601, Australia
Dr. C. Xiong
School of Chemistry and Environmental Engineering
Shenzhen University
Shenzhen 518060, China
The ORCID identification number(s) for the author(s) of this article can be found under https://doi.org/10.1002/smll.202002343.

DOI: 10.1002/smll.202002343

© 2020 WILEY-VCH Verlag GmbH & Co. KGaA, Weinheim

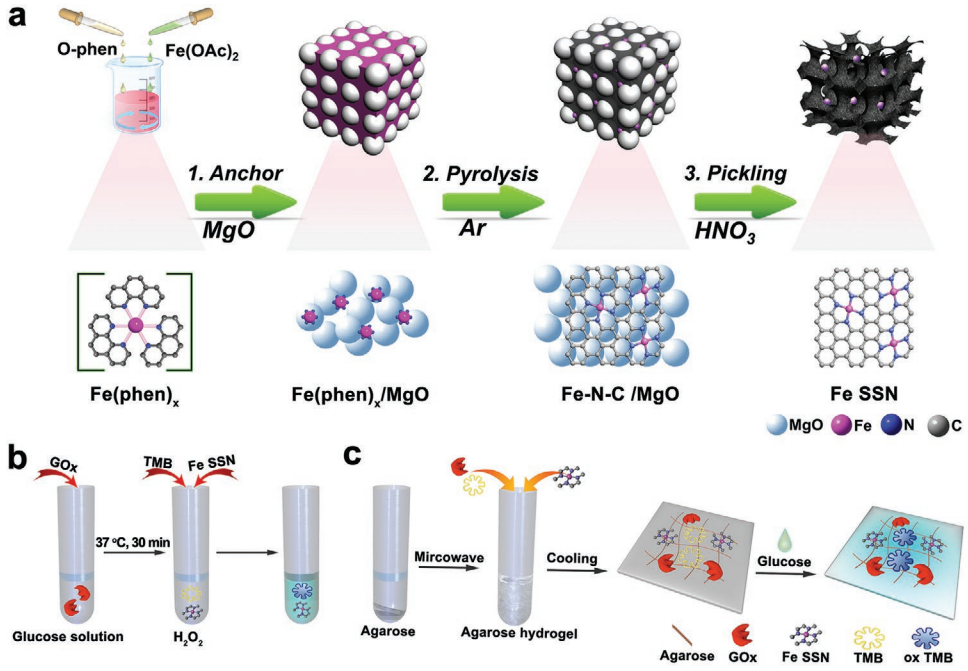

Figure 1. a) The schematic illustration for the preparation of Fe SSN. b) Modified colorimetric detection of glucose. c) Integrated agarose-based hydrogel colorimetric detection of glucose.

peroxidase-like nanozymes-glucose oxidase (GO_x) biocatalytic cascade platform (Figure 1b).[23] Generally, peroxidase-like nanozymes and TMB should be added in solution after the complete GO_x-catalyzed glucose oxidation, which needs complicated analytical procedure and extended time.[24] Thus, we fabricated a simple, sensitive, and low-cost integrated colorimetric biosensor by embedding all biosensing ingredients (TMB, GO_x, and Fe SSN) into the agarose-based hydrogel (Figure 1c), which is proved to realize the reliable visualization evaluation and quantitative detection of glucose rapidly and easily. This work not only introduces an innovative peroxidase-like SSC, but also provides feasibility to realize the point-of-care detection of glucose in complex bioassay like serum.

The transmission electron microscopy (TEM) (**Figure 2**a; Figure S2, Supporting Information) and scanning transmission electron microscopy (STEM) (Figure 2b; Figure S3, Supporting Information) images show that there are no visible particles in Fe SSN. Meanwhile the sample is extremely thin and the loose sheet is full of many different sizes of holes. As revealed by N_2 adsorption–desorption curves and pore size distributions (Figure S4, Supporting Information), the sample exhibits a large surface area (578 $m^2\ g^{-1}$) and contains abundant micro- and mesopores, contributing to anchoring active Fe atoms and mass transfer, well corresponding to the TEM results. Moreover, the energy dispersive X-ray spectroscopy (EDS) mappings indicate that Fe, N, and C are uniformly dispersed (Figure 2c). In order to further explore the structure of the catalyst and the existence form of Fe, we used the aberration-corrected high angle annular dark-field scanning transmission electron microscope (HAADF-STEM) to test. HAADF-STEM images of Fe SSN reveal that the small dense bright dots assigned to single Fe sites are in homogeneous atomic dispersion (Figure 2d,e; Figure S4, Supporting Information). Some Fe single atoms are marked with red circles for better observation. 3D isolines (Figure 1f) and atom-overlapping Gaussian-function fitting mapping (Figure 1g) of the square from Figure 1e further show that the surface N-doped carbon substrate is decorated by the heavier Fe atoms. In addition, the intensity profile along X–Y in Figure 1e displays that Fe atoms are separated by at least 0.35 nm (Figure 1h), which is slightly larger than the lattice distance of Fe (100) facet (d_{100} = 0.235 nm). By inductively coupled plasma atomic emission spectroscopy test (ICP-AES), the actual Fe loading of Fe SSN is detected to 1.06 wt%.

The X-ray diffraction (XRD) pattern (**Figure 3**a) shows no corresponding diffraction peaks of Fe crystals in Fe SSN, eliminating the generation of Fe-related particles. As can be seen from the Raman spectra (Figure S6, Supporting Information), only G band and D band at 1600 and 1350 cm^{-1} are observed, further revealing no formation of any FeO_x species in the sample.[25] The X-ray photoelectron spectroscopy (XPS) and the extended X-ray absorption fine structure (EXAFS) were carried out to further investigate the electronic structure and coordination environment of Fe SSN. XPS result demonstrates that Fe SSN is composed of Fe, N, and C (Figure S7, Supporting Information). For Fe SSN, there are two peaks of Fe at 711.3 and 724.5 eV, unveiling the ionic $Fe^{\delta+}$ ($\delta \approx 3$) nature of Fe in Fe SSN.[26] As seen in Figure S7b (Supporting Information), Fe SSN obtains much high defective N configurations, like pyridinic N and pyrrolic N, which are recognized as anchor points for single Fe atom.[27] It suggests that Fe SSN has abundant active Fe-N_x sites. The X-ray absorption near-edge structure (XANES) spectra (Figure 3b) show that the absorption threshold position of Fe SSN located between those of FeO and Fe_2O_3, revealing the valence state of $Fe^{\delta+}$ ($2 < \delta < 3$) in Fe SSN. This observation is in accord with the aforementioned XPS results. The Fourier transform (FT) k^3-weighted $\chi(k)$ function of the EXAFS spectra of Fe SSN display a dominant peak at

© 2020 WILEY-VCH Verlag GmbH & Co. KGaA, Weinheim

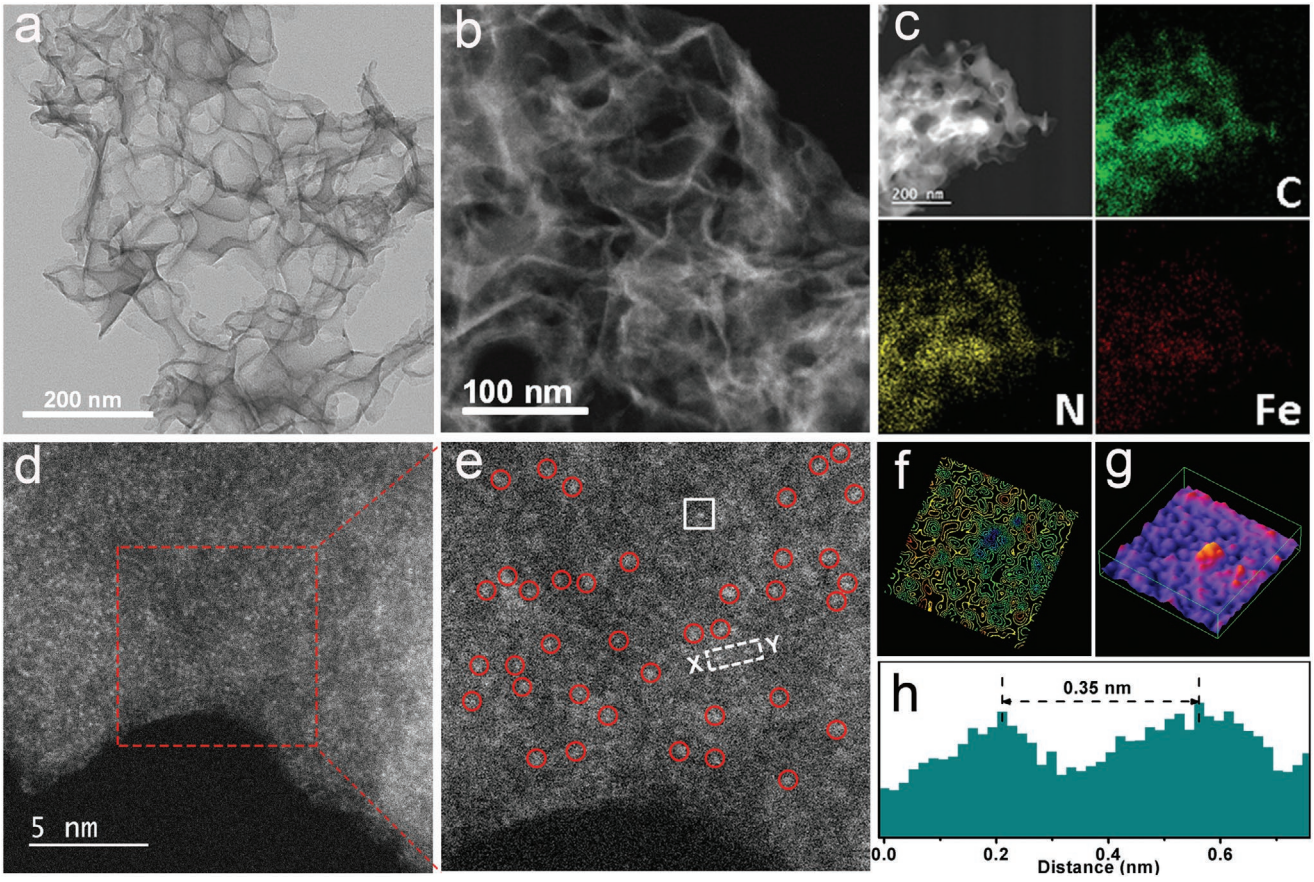

Figure 2. a) TEM image of Fe SSN. b) DF-STEM image of Fe SSN. c) Corresponding EDS maps revealing the homogeneous distribution of Fe and N on porous carbon support. d,e) Magnified HAADF-STEM images of Fe SSN. The Fe single atoms are marked with red circles. f) 3D isolines and g) atom-overlapping Gaussian-function fitting mapping of the square from (e). h) Intensity profiles along *X*–*Y* in the magnified AC HAADF-STEM image in (e).

1.49 Å, corresponding to the Fe–N coordination (Figure 3c), which confirm the atomic dispersion of single Fe sites in Fe SSN. To better illustrate the active sites, we further calculated the corresponding Fe K-edge EXAFS fitting curves of the Fe SSN and found out the coordination number of Fe–N is about 4 and the average bond length of Fe–N is 2.04 Å. The FT-EXAFS fitting results are shown in Figure 3d and Figure S19 and Table S1 in the Supporting Information. Based on the above results, Fe SSN with uniform Fe-N_4 sites, robust structure and large surface area is expected to be an ideal nanozyme with superior activity and stability.

The peroxidase-mimicking activity investigation of Fe SSN was executed in the H_2O_2-TMB chromogenic system. In the presence of Fe SSN and H_2O_2, the colorless TMB turns to blue with an absorption peak emerging at 652 nm. To evaluate the catalytic activity of Fe SSN, we performed the steady-state kinetics in acetate buffer (0.1 M, pH 4.0) at 37 °C in a certain range of H_2O_2 and TMB concentrations (Figure S9, Supporting Information). Typical UV–vis absorption spectra are shown in **Figure 4**a and Figure S10a (Supporting Information) for different concentrations of H_2O_2 and TMB respectively. The maximal reaction velocity (V_{max}) and Michaelis–Menten constant (K_m) of Fe SSN are obtained from the Lineweaver–Burk plots via Michaelis–Menten equation (Figure 4b; Figure S10, Supporting Information).[6] K_m, which indicates the enzyme affinity of substrates,[28] is determined as 0.36×10^{-3} M for H_2O_2 (Table S3, Supporting Information), ten times lower than that of horseradish peroxidase (HRP), suggesting the superior capacity for activating H_2O_2. The V_{max} of the Fe SSN with the TMB substrate or the H_2O_2 substrate is two times higher than that of HRP, indicative of the Fe SSN having a higher catalytic ability than HRP, which is mainly contributed to its uniform Fe-N_4 sites similar with natural heme-containing enzymes. Moreover, compared with recent single-atom nanozymes,[29–32] K_m of Fe SSN to TMB or H_2O_2 is smaller than most of them. As for V_{max}, Fe SSN is comparable to these catalysts, while substrate concentration and catalyst dosage are much smaller than them, which suggests that Fe SSN exhibits markedly higher peroxidase mimic. Then, we investigated the effects of solution temperature and buffer pH on the peroxidase-like reaction of Fe SSN. As described in Figure S8 (Supporting Information), the best temperature is about 44 °C and the optimal pH is 4.0. To check the stability of Fe SSN, we studied its ability to resist harsh pH and temperature as well as its storage stability. The results suggest that Fe SSN shows excellent robustness in different pH (3.0–8.0) or at various temperatures (4–80 °C) (Figure S11, Supporting Information) and the peroxidase-like activity of Fe SSN does not decrease when Fe SSN is stored at room temperature for 12 d (Figure S16a, Supporting Information). We also compared the performance of Fe SSN prepared six months ago with that of the freshly prepared (Figure S16b,

© 2020 WILEY-VCH Verlag GmbH & Co. KGaA, Weinheim

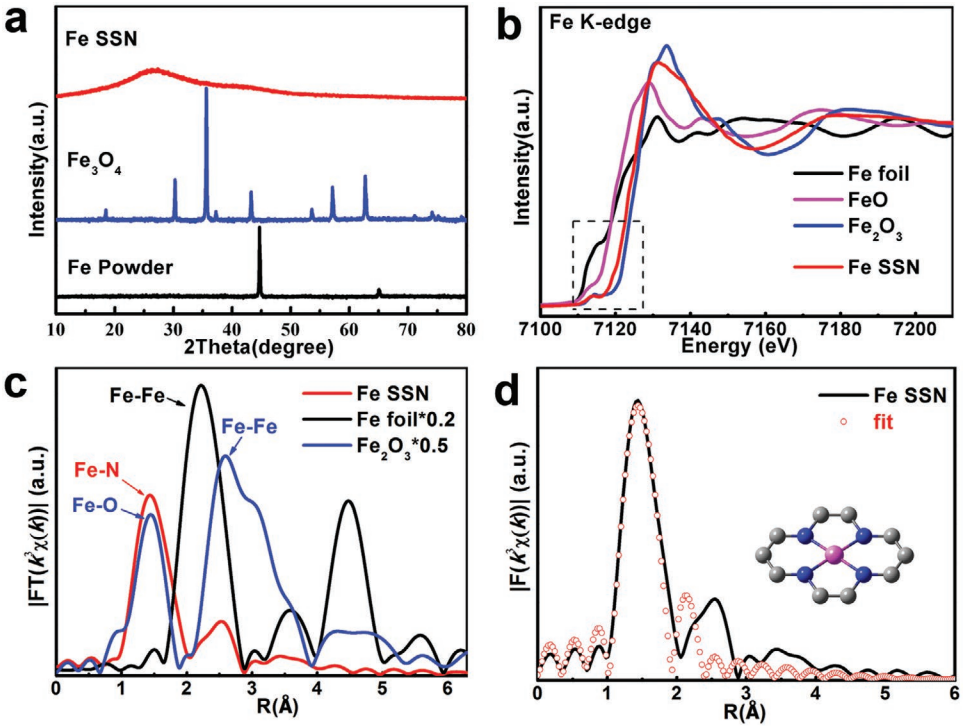

Figure 3. a) XRD patterns of Fe SSN, Fe_3O_4, and Fe powder. b) Fe K-edge XANES spectra. c) k^3-weighted $\chi(k)$ function of the EXAFS spectra. d) Corresponding FT-EXAFS fitting curves of Fe SSN. The pink, blue, and gray balls represent the Fe, N, and C atoms, respectively.

Supporting Information) and found that the activity was only reduced by 20%, which verifies its stability. Furthermore, the morphology of Fe SSN after the catalysis shows no significant alterations in TEM and STEM images (Figure S12, Supporting Information), and the HAADF-STEM images of Fe SSN (Figure S13, Supporting Information) reveal that Fe atoms still present homogeneous atomic dispersion after the catalysis, further proving its stability.

To explore the origin of the superior peroxidase-mimicking property of Fe SSN, we performed electron paramagnetic resonance (EPR) experiments to detect the generating radicals during the catalytic process. Generally, 5, 5-dimethyl-1-pyrroline *N*-oxide (DMPO) is used for catching radicals in the reaction. As can be seen from Figure 4c, there are four peaks in the EPR spectrum when Fe SSN meets with H_2O_2, and the corresponding intensity ratio is 1:2:2:1, which is in good consistent with DMPO-•OH. This result strongly verifies that the Fe-N_4 on the surface of Fe SSN function as peroxidase-like active sites for oxidation of TMB.

Based on the outstanding peroxidase-mimicking property of Fe SSN, we first used the Fe SSN-GO_x-TMB system to detect glucose in solution (Figure 1b). As the glucose concentration increases from 10 to 200 × 10^{-6} M, the absorbance at 652 nm rises accordingly, along with an obvious color variation from colorless to blue (Figure 4d,e). The Fe SSN-GO_x-TMB system is able to detect glucose ranging from 10 to 60 × 10^{-6} M in a good linearity, with a limit of detection (LOD) (S/N = 3) as low as 2.1 × 10^{-6} M (Figure 4e), which is superior to most reported colorimetric detection for glucose (Table S3, Supporting Information) and is sufficient to applied in practical glucose sample monitoring. Furthermore, the selectivity of Fe SSN-GO_x-TMB system was divided into the selectivity of Fe SSN to H_2O_2 and the selectivity of the system to glucose by observing the responses toward the common interfering chemicals. In the case of the same substrate concentration, compared with the common metal ions and TMB, only H_2O_2 causes the response of Fe SSN, indicating its high selectivity to H_2O_2 (Figure S17, Supporting Information). As illustrated in Figure 4f, only glucose produces significant change in solution color whereas the above interfering chemicals stay colorless the same as blank, strongly suggesting the high selectivity for glucose. Moreover, in the presence of the interfering molecules, the absorbances are basically the same as that of glucose alone (Figure S18, Supporting Information), which further proves the selectivity of the system. Such high selectivity is mainly due to GO_x.

To broaden the practicality of the Fe SSN-GO_x-TMB colorimetric biosensing system especially in point-of-care detection, we designed an integrated agarose-based hydrogel colorimetric biosensor containing 100 µL GO_x (10 mg mL^{-1}), 800 µL TMB solution (6 × 10^{-6} M), and 100 µL of Fe SSN (1 mg mL^{-1}). The gelation process can be seen in Figure 1c. We then investigated the changes of absorption spectra and the corresponding color by dropping different glucose concentrations on the above hydrogel film. As shown in Figure 4g,h, the hydrogel film varies from colorless to blue gradually as the glucose concentration rising from 0.3 to 10 × 10^{-3} M, accompanied with the increase of absorbance at 652 nm. A good linear correlation is also obtained ranging from 0.3 to 3.0 × 10^{-3} M (Figure 4i). However, when the glucose concentration is below 0.3 × 10^{-3} M, there are no distinctions in the color and absorption spectra of the hydrogel films compared

© 2020 WILEY-VCH Verlag GmbH & Co. KGaA, Weinheim

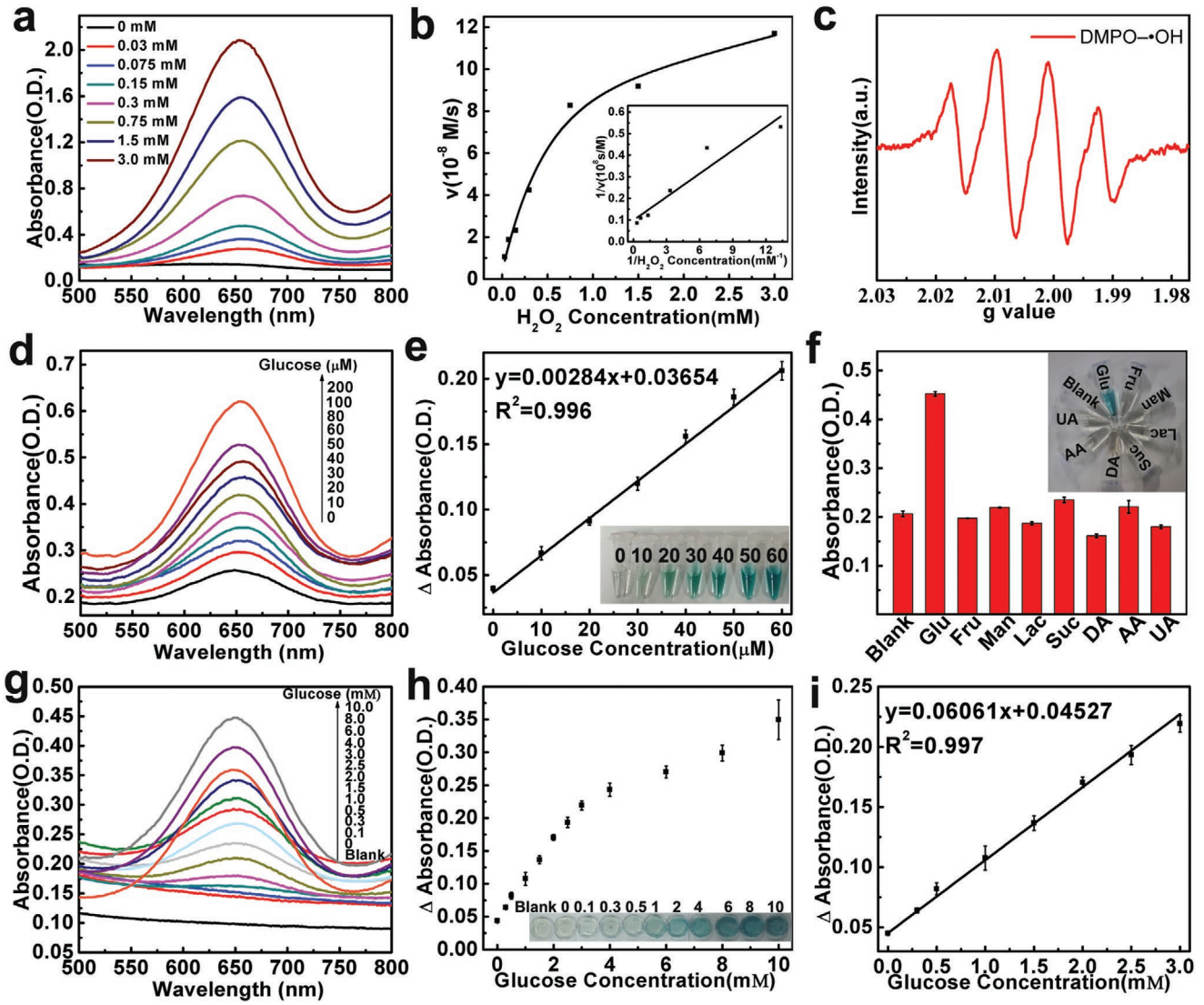

Figure 4. a–c) Peroxidase-mimicking activity of Fe SSN. a) The UV–vis absorption spectra of Fe SSN in different H_2O_2 concentrations. b) Michaelis–Menten kinetics curves. Inset: Lineweaver–Burk plots. c) EPR spectrum detected in peroxidase-like activity of Fe SSN. d–f) Modified colorimetric detection of glucose by the Fe SSN-GOx-TMB system. d) UV–vis absorption spectra of Fe SSN in different glucose concentrations. e) Linear calibration curve of the absorbance at 652 nm against glucose concentration. f) Selectivity toward glucose of the above system against potential interfering substances. All the concentrations were 50×10^{-6} M. g–i) Visualization of glucose levels using integrated agarose-based hydrogel colorimetric biosensor containing GOx, TMB, and Fe SSN. g) UV–vis absorption spectra of Fe SSN in different glucose concentrations. h) The absorbance at 652 nm against glucose concentration. i) Linear calibration curve of the absorbance at 652 nm against glucose concentration.

with 0×10^{-3} M assay (Figure 4h,g). Even though, it could be still applied in glucose detection in human serum. Hence, to lower its LOD, we doubled the amount of GO_x and Fe SSN in the agarose-based hydrogel. The color evolution during the detection can be seen in Figure S14 in the Supporting Information. This enhanced hydrogel film is able to detect glucose in a good linear range of 10–100 $\times 10^{-3}$ M. The color change still cannot be distinguished by naked eyes whereas the distinctions in absorbance at 652 nm can be monitored by spectrophotometer (Figure S15, Supporting Information), and the LOD (S/N = 3) is 8.2×10^{-6} M, transcending most reported colorimetric biosensors for glucose detection (Table S3, Supporting Information).

In summary, we developed a support-sacrificed approach to prepare a novel single site nanozyme denoted as Fe SSN. Compared with the reported SSCs and other Fe-based nanozymes, the Fe SSN performed ascendant peroxidase-mimicking activity and favorable stability against harsh conditions due to its uniform $Fe\text{-}N_4$ active sites, large surface area and robust structure. After achieving the accurate glucose colorimetric detection in solution via Fe SSN-GO_x-TMB system, we established a low-cost integrated agarose-based hydrogel colorimetric biosensor which successfully realizes the visualization and quantitative evaluation for glucose. Our findings not only introduce a new horizon for developing SSC-based biosensors but also pave an avenue for point-of-care detection of glucose in biomedical diagnosis.

© 2020 WILEY-VCH Verlag GmbH & Co. KGaA, Weinheim

Experimental Section

The details of experiments can be seen in Supporting Information.

Supporting Information

Supporting Information is available from the Wiley Online Library or from the author.

Acknowledgements

This work was supported by National Key R&D Program of China 2017YFA (0208300) and (0700104), the Postdoctoral Science Foundation of China (2019M653052), the National Natural Science Foundation of China (21671180). The authors thank the photoemission endstations BL1W1B in Beijing Synchrotron Radiation Facility (BSRF), BL14W1 in Shanghai Synchrotron Radiation Facility (SSRF), BL10B and BL11U in National Synchrotron Radiation Laboratory (NSRL) for the help in characterizations.

Conflict of Interest

The authors declare no conflict of interest.

Keywords

glucose detection, hydrogel colorimetric biosensors, peroxidase-like activity, single iron site nanozymes

Received: April 12, 2020
Revised: May 21, 2020
Published online:

[1] Y. Lin, J. Ren, X. Qu, *Acc. Chem. Res.* **2014**, *47*, 1097.
[2] Y. Zhou, B. Liu, R. Yang, J. Liu, *Bioconjugate Chem.* **2017**, *28*, 2903.
[3] H. Wei, E. Wang, *Chem. Soc. Rev.* **2013**, *42*, 6060.
[4] N. A. Kotov, *Science* **2010**, *330*, 188.
[5] A. Asati, S. Santra, C. Kaittanis, S. Nath, J. M. Perez, *Angew. Chem., Int. Ed.* **2009**, *48*, 2308.
[6] L. Gao, J. Zhuang, L. Nie, J. Zhang, Y. Zhang, N. Gu, T. Wang, J. Feng, D. Yang, S. Perrett, *Nat. Nanotechnol.* **2007**, *2*, 577.
[7] Y. Huang, Z. Liu, C. Liu, E. Ju, Y. Zhang, J. Ren, X. Qu, *Angew. Chem., Int. Ed.* **2016**, *55*, 6646.
[8] W. Li, Z. Liu, C. Liu, Y. Guan, J. Ren, X. Qu, *Angew. Chem., Int. Ed.* **2017**, *56*, 13661.
[9] B. Liu, Z. Huang, J. Liu, *Nanoscale* **2016**, *8*, 13562.
[10] K. Fan, J. Xi, L. Fan, P. Wang, C. Zhu, Y. Tang, X. Xu, M. Liang, B. Jiang, X. Yan, L. Gao, *Nat. Commun.* **2018**, *9*, 1440.
[11] X. Wang, C. Hou, W. Qiu, Y. Ke, Q. XuX. Y. Liu, Y. Lin, *ACS Appl. Mater. Interfaces* **2017**, *9*, 684.
[12] K. Fan, H. Wang, J. Xi, Q. Liu, X. Meng, D. Duan, L. Gao, X. Yan, *Chem. Commun.* **2017**, *53*, 424.
[13] W. Bing, H. Sun, F. Wang, Y. Song, J. Ren, *J. Mater. Chem. B* **2018**, *6*, 4602.
[14] B. Liu, J. Liu, *Nano Res.* **2017**, *10*, 1125.
[15] S. Liu, F. Lu, R. Xing, J. Zhu, *Chem. - Eur. J.* **2011**, *17*, 620.
[16] X. Xia, J. Zhang, N. Lu, M. J. Kim, K. Ghale, Y. Xu, E. McKenzie, J. Liu, H. Ye, *ACS Nano* **2015**, *9*, 9994.
[17] B. Qiao, A. Wang, X. Yang, L. F. Allard, Z. Jiang, Y. Cui, J. Liu, J. Li, T. Zhang, *Nat. Chem.* **2011**, *3*, 634.
[18] P. Yin, T. Yao, Y. Wu, L. Zheng, Y. Lin, W. Liu, H. Ju, J. Zhu, X. Hong, Z. Deng, G. Zhou, S. We, Y. Li, *Angew. Chem., Int. Ed.* **2016**, *55*, 10800.
[19] W. Liu, L. Zhang, X. Liu, X. Liu, X. Yang, S. Miao, W. Wang, A. Wang, T. Zhang, *J. Am. Chem. Soc.* **2017**, *139*, 10790.
[20] L. Ai, L. Li, C. Zhang, J. Fu, J. Jiang, *Chem. - Eur. J.* **2013**, *19*, 15105.
[21] L. Huang, J. Chen, L. Gan, J. Wang, S. Dong, *Sci. Adv.* **2019**, *5*, eaav5490.
[22] L. Jiao, H. Yan, Y. Wu, W. Gu, C. Zhu, D. Du, Y. Lin, *Angew. Chem., Int. Ed.* **2020**, *59*, 2565.
[23] Y. Song, K. Qu, C. Zhao, J. Ren, X. Qu, *Adv. Mater.* **2010**, *22*, 2206.
[24] J. Feng, P. Huang, F. Wu, *Analyst* **2017**, *142*, 4106.
[25] G. Wu, C. M. Johnston, N. H. Mack, K. Artyushkova, M. Ferrandon, M. Nelson, J. S. Lezama-Pacheco, S. D. Conradson, K. L. More, D. J. Myers, P. Zelenay, *J. Mater. Chem.* **2011**, *21*, 11392.
[26] X. Chen, Y. Zhao, G. Fu, P. N. Duchesne, L. Gu, Y. Zheng, X. Weng, M. Chen, P. Zhang, C. Pao, J. - F. Lee, N. Zheng, *Science* **2014**, *344*, 495.
[27] H. W. Liang, S. Bruller, R. Dong, J. Zhang, X. Feng, K. Mullen, *Nat. Commun.* **2015**, *6*, 7992.
[28] Y. Tao, Y. Lin, Z. Huang, J. Ren, X. Qu, *Adv. Mater.* **2013**, *25*, 2594.
[29] C. Zhao, C. Xiong, X. Liu, M. Qiao, Z. Li, T. Yuan, J. Wang, Y. Qu, Y. Wu, Y. Li, *Chem. Commun.* **2019**, *55*, 2285.
[30] B. Xu, H. Wang, W. Wang, L. Gao, S. Li, X. Pan, H. Wang, H. Yang, X. Meng, Q. Wu, L. Zheng, S. Chen, X. Shi, K. Fan, X. Yan, H. Liu, *Angew. Chem., Int. Ed.* **2019**, *58*, 4911.
[31] N. Cheng, J. C. Li, D. Liu, Y. Lin, D. Du, *Small* **2019**, *15*, 1901485.
[32] L. Jiao, W. Xu, H. Yan, Y. Wu, C. Liu, D. Du, Y. LinC. Zhu, *Anal. Chem.* **2019**, *91*, 11994.

 © 2020 WILEY-VCH Verlag GmbH & Co. KGaA, Weinheim